

Restoring universality to the pinch-off of a bubble

Amir A. Pahlavan^{a,b,1}, Howard A. Stone^b, Gareth H. McKinley^a, and Ruben Juanes^{c,d,1}

^aDepartment of Mechanical Engineering, Massachusetts Institute of Technology, Cambridge, MA 02139; ^bDepartment of Mechanical and Aerospace Engineering, Princeton University, Princeton, NJ 08540; ^cDepartment of Civil and Environmental Engineering, Massachusetts Institute of Technology, Cambridge, MA 02139; and ^dDepartment of Earth, Atmospheric and Planetary Sciences, Massachusetts Institute of Technology, Cambridge, MA 02139

Edited by Osman A. Basaran, Purdue University, West Lafayette, IN, and accepted by Editorial Board Member John D. Weeks May 13, 2019 (received for review November 19, 2018)

The pinch-off of a bubble is an example of the formation of a singularity, exhibiting a characteristic separation of length and time scales. Because of this scale separation, one expects universal dynamics that collapse into self-similar behavior determined by the relative importance of viscous, inertial, and capillary forces. Surprisingly, however, the pinch-off of a bubble in a large tank of viscous liquid is known to be nonuniversal. Here, we show that the pinch-off dynamics of a bubble confined in a capillary tube undergo a sequence of two distinct self-similar regimes, even though the entire evolution is controlled by a balance between viscous and capillary forces. We demonstrate that the early-time self-similar regime restores universality to bubble pinch-off by erasing the system's memory of the initial conditions. Our findings have important implications for bubble/drop generation in microfluidic devices, with applications in inkjet printing, medical imaging, and synthesis of particulate materials.

bubble pinch-off | finite-time singularity formation | universality | moving contact lines

From dripping faucets to children blowing soap bubbles, we observe the formation of drops and bubbles on a daily basis. This seemingly simple phenomenon, however, has long puzzled and attracted scientists, from the early descriptions of da Vinci, Savart, Plateau, and Rayleigh (1–3) to advanced experimental techniques that yield precise observations of the interface evolution leading to pinch-off (4–9). Most previous studies of singularities during bubble or drop formation have focused on unbounded fluid domains (10–17). Many natural phenomena and industrial processes, however, often involve flows under confinement (18–23), where the dimensionality of the confined geometry is known to strongly influence the pinch-off (24–28). These studies have assumed that a continuous liquid phase coats all of the bounding surfaces. In many situations, however, one encounters partially wetting liquids, which naturally lead to the presence of contact lines, where a fluid–fluid interface meets the solid surface (29).

Here, we study the pinch-off of a bubble in confinement in the partial wetting regime. We show that the moving contact line singularity (30, 31) dominates the viscous dissipation at early times, leading to an axially dominated flow and the emergence of an early-time self-similar regime, which then crosses over to a late-time regime, where the flow is mainly radial and the viscous dissipation is dominated by the pinch-off singularity. While the observation of different self-similar regimes is expected when the balance of forces between inertia, viscosity, and capillarity changes (11, 32, 33), here we show that in our system, the cross-over between self-similar regimes occurs even though the entire evolution is controlled by a balance between viscous and capillary forces.

The separation of length and time scales in the vicinity of a singularity suggests that the local balance of forces should become independent of the details of the initial or boundary conditions, making the dynamics of the pinch-off universal (10). Surprisingly, in the case of the pinch-off of an inviscid bubble in an unbounded ambient viscous liquid, the local structure of the singularity is sensitive to the details of the experimental conditions, render-

ing the pinch-off nonuniversal (13, 34–36). Here, we show that the presence of the early-time regime in a confined geometry establishes the tube diameter as the only length scale in the problem and erases the system's memory of the experimental details and initial conditions, leading to the universality of the bubble pinch-off.

We study the bubble generation process in a microcapillary tube (diameter $d = 280, 750 \mu\text{m}$). The tube is connected to a syringe pump on one end and is open to the atmosphere on the other end (Fig. 1). We first fill the tube with a water–glycerol mixture (viscosity $\mu = 0.2$ or $1.4 \text{ Pa}\cdot\text{s}$ depending on composition, and surface tension $\gamma = 65 \text{ mN/m}$) that is partially wetting to the tube ($\theta_{eq} \approx 65^\circ$) and then start withdrawing the liquid using the pump at a specified flow rate Q . At low flow rates, the meniscus deforms slightly and moves downstream at a constant velocity $U = 4Q/(\pi d^2)$. When the imposed flow rate is higher than a critical value, however, a wetting transition occurs: the meniscus loses its quasi-static geometry and air starts invading the tube in the form of an extending axial finger, leaving a film of the viscous liquid on the walls (37). Fig. 1 shows that the entrained liquid film immediately starts to dewet along the tube walls. As the contact line recedes, the rim ahead of it grows and the bubble neck shrinks until it finally pinches off and forms a bubble (Movie S1).

In the case of bubble formation in a large quiescent tank, the balance of radial viscous flow and surface tension causes the bubble neck diameter to shrink linearly in time (35, 38). In contrast, here, during the process of bubble pinch-off in a

Significance

We observe the formation of bubbles and drops on a daily basis, from dripping faucets to raindrops entraining bubbles on the surface of a lake. The ubiquity of the phenomenon masks the fascinating underlying nonlinear dynamics that is such an important aspect of modern physics. Here, we report on the surprising observation that confinement makes the pinch-off of a bubble a universal process, as opposed to the unconfined case, where pinch-off is sensitive to the details of the experimental setting. We explain how the motion of the contact line, where the liquid, gas, and solid phases meet, leads to self-similar dynamics that effectively erase the memory of the system. Our observations have implications for immiscible flow phenomena from microfluidics to geophysical flows, where confinement, together with fluid–solid physicochemical interactions, play a key role.

Author contributions: A.A.P. and R.J. designed research; A.A.P. performed research; A.A.P., H.A.S., G.H.M., and R.J. analyzed data; and A.A.P., H.A.S., G.H.M., and R.J. wrote the paper.

The authors declare no conflict of interest.

This article is a PNAS Direct Submission. O.A.B. is a Guest Editor invited by the Editorial Board.

Published under the PNAS license.

¹To whom correspondence may be addressed. Email: pahlavan@princeton.edu or juanes@mit.edu.

This article contains supporting information online at www.pnas.org/lookup/suppl/doi:10.1073/pnas.1819744116/-DCSupplemental.

Published online June 17, 2019.

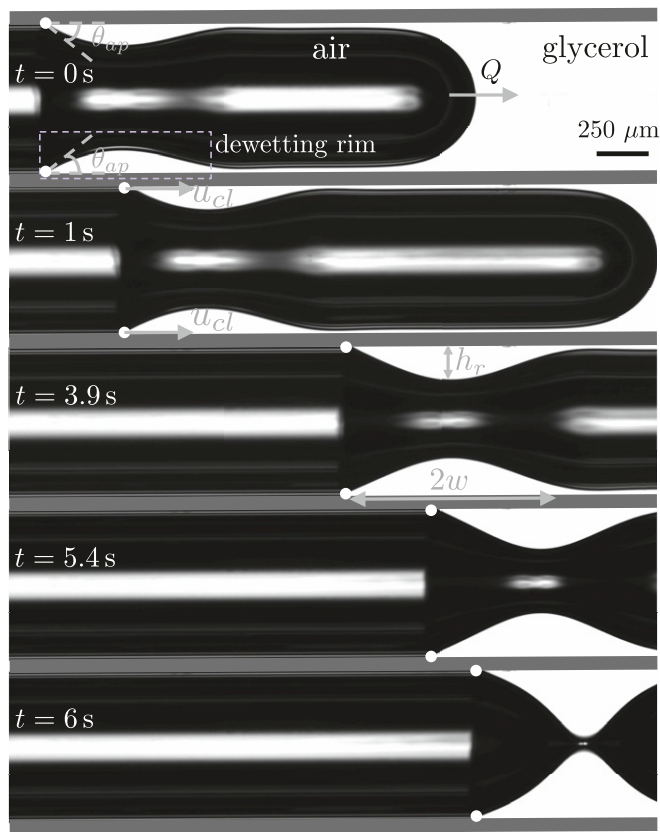


Fig. 1. Displacement of a partially wetting liquid from a microcapillary tube. As the glycerol (white) is withdrawn from the right end of the tube with a constant flow rate Q , air (black) invades the tube from the left end at atmospheric pressure and entrains a thin film of the glycerol on the tube walls (the white stripe in the middle of the tube is due to light refraction; [SI Appendix, section 1](#)). The entrained liquid film then starts receding along the tube axis with a velocity U_{cl} , forming a growing dewetting rim ahead of the contact line, where the liquid, solid, and air meet at a nonzero apparent contact angle θ_{ap} . As the liquid rim grows, the bubble neck diameter shrinks and ultimately leads to pinch-off and the formation of a bubble.

microcapillary tube, the evolution of the diameter of the bubble neck indicates the presence of two distinct self-similar regimes (Fig. 24), as illustrated with the results from 12 different experiments: the bubble neck diameter initially follows a $\tau^{1/5}$ scaling before transitioning to the familiar linear scaling regime, where $\tau = (t_0 - t)$ is the time to the singularity with t_0 as the pinch-off time (Fig. 2B). The Reynolds number is defined as $Re = \rho U l / \mu$, where ρ is the liquid density, and U and l are the characteristic velocity and length scales. At early times, the characteristic velocity and length scales are set by the moving contact line and the tube diameter, leading to $U \sim U_{cl} \sim (\gamma/\mu)\theta_{eq}^3$ and $l \approx h_r^2/w$, where h_r and w represent the height and width of the dewetting rim, respectively (Fig. 1). At late times, in the vicinity of the pinch-off, the bubble neck can be idealized as a cylindrical thread of radius r_0 that is shrinking in time, leading to $U \sim dr_0/d\tau$ and $l \sim r_0$. During the entire evolution, $Re \ll 1$ and inertia can be neglected.

To gain an understanding of this early-time self-similar regime for the time evolution of the bubble radius, we consider the dynamics of the growing dewetting rim (Fig. 1). This can be analyzed using a long-wave approximation (37), which assumes that the flow is mainly parallel to the tube axis. Near the point of pinch-off, we postulate that the shape of the profile becomes self-similar: $\tilde{R}(\xi) = \tilde{r}(\tilde{z}, \tilde{\tau})/\tilde{\tau}^\alpha$, and $\xi = (\tilde{z} - \tilde{z}_0)/\tilde{\tau}^\beta$

with α and β as constants (Fig. 24, *Inset*); here, all of the length scales are nondimensionalized by the tube diameter d , and the dimensionless time to the singularity is defined as $\tilde{\tau} = \tau/t^*$, where $t^* = \mu d/\gamma$ is the visco-capillary time scale. Unlike the inertia-viscocapillary regime, where fluid properties introduce an intrinsic length scale into the problem $l_v = \mu^2/\gamma\rho$ (10), the visco-capillary regime discussed here requires an external length scale—the tube diameter d . Using this ansatz, we arrive at an ordinary differential equation for the neck profile ([SI Appendix, section 2](#)):

$$(-\alpha\tilde{R} + \beta\xi\tilde{R}')\tilde{\tau}^{\alpha-1} = \frac{1}{(16)^2} \frac{1}{\tilde{R}} \left(\left[-\frac{2}{\tilde{R}^3} \tilde{R}'^2 + \frac{1}{\tilde{R}^2} \tilde{R}'' \right] \tilde{\tau}^{-2(\alpha+\beta)} + \tilde{R}''' \tilde{\tau}^{-4\beta} \right), \quad [1]$$

where primes indicate differentiation with respect to ξ . The left-hand side of Eq. 1 represents the viscous forces, and the right-hand side represents the capillary forces: the first two terms represent the out-of-plane curvature and the last term represents the in-plane curvature. The only way for all of the terms to balance in time is to have $\alpha = \beta = 1/5$, leading to $\tilde{R}(\xi) = \tilde{r}(\tilde{z}, \tilde{\tau})/\tilde{\tau}^{1/5}$, and $\xi = (\tilde{z} - \tilde{z}_0)/\tilde{\tau}^{1/5}$. This result is consistent with the experimentally observed scaling of the neck diameter as a function of time to pinch-off in the early-time self-similar regime shown in Fig. 2B. The self-similar ordinary differential equation governing the neck profile in the early-time regime therefore has the following form:

$$(-\tilde{R} + \xi\tilde{R}') = \frac{5}{(16)^2} \frac{1}{\tilde{R}} \left(\left[-\frac{2}{\tilde{R}^3} \tilde{R}'^2 + \frac{1}{\tilde{R}^2} \tilde{R}'' \right] + \tilde{R}''' \right). \quad [2]$$

The early-time self-similar regime is an example of self-similarity of the first kind, in which the scaling exponents can be uniquely determined based on dimensional analysis (39), as outlined above. The cross-over to the late-time self-similar regime, however, hints at the breakdown of the long-wave model very close to the point of pinch-off.

An important point here is that the long-wave approximation is developed for the dewetting rim, and not for the bubble neck. The relevant length scales are therefore the height (h_r) and width ($2w$) of the dewetting rim (Fig. 1), the ratio of which determines the apparent contact angle as $\theta_{ap} = 2h_r/w \approx 30^\circ$, which is small enough for the long-wave approximation to be valid (40, 41). This observation is further confirmed in our earlier work, showing an excellent match between the experimentally observed profiles and the theoretical prediction (37). Of course, the long-wave approximation ultimately breaks down as the slope of the meniscus near the point of singularity diverges, leading to a cross-over to the late-time self-similar regime. While both regimes are governed by a balance of capillary and viscous forces, the cross-over occurs due to a change in the nature of the viscous flow in the dewetting film from axially dominated to radially dominated, as the dominant dissipative process changes from the moving contact line singularity to the pinch-off singularity ([Movie S2](#)).

To estimate the cross-over time between the two regimes, we compare their corresponding radial velocities. In the early-time regime, the growth rate of the dewetting rim is proportional to the velocity of the receding contact line, i.e., $dr_0/d\tau \sim U_{cl} \sim (\gamma/\mu)\theta_{eq}^3$, which is nearly constant for a given wettability (37, 41). In the late-time regime, the thin bubble neck close to the point of singularity can be approximated as an axisymmetric cylinder, and the flow in the outer viscous fluid can be approximated as purely radial. The normal viscous stress generated by the radial flow is balanced by surface tension, leading to $dr_0/d\tau \sim (\gamma/\mu)e^{-\tau/t^*}$ as an estimate for the radial velocity in the late-time regime ([SI Appendix, section 3](#)). Note that very close to the point of pinch-off ($\tau/t^* \ll 1$), we recover the familiar linear scaling in

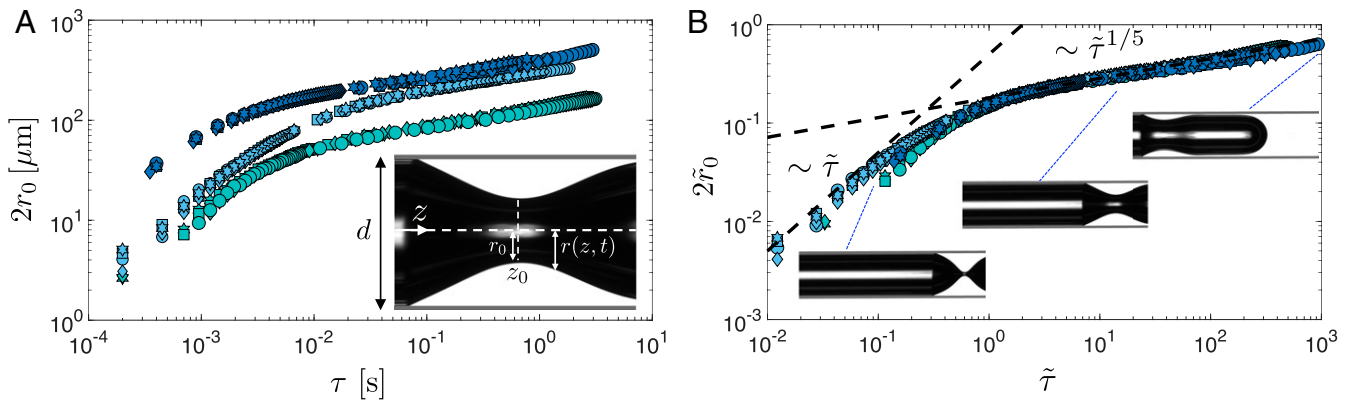


Fig. 2. Evolution of the neck diameter versus time $\tau = (t_0 - t)$ to pinch-off at t_0 . (A) Data from 12 different experiments are shown: light blue symbols correspond to $d = 750 \mu\text{m}$ and $\mu = 1.4 \text{ Pa.s}$; the cyan symbols correspond to $d = 280 \mu\text{m}$ and $\mu = 1.4 \text{ Pa.s}$; the dark blue symbols correspond to $d = 750 \mu\text{m}$ and $\mu = 0.2 \text{ Pa.s}$. Each color represents data corresponding to four different flow rates with $\text{Ca} = \mu U / \gamma \in [0.008, 0.02]$, where $U = 4Q / (\pi d^2)$ and Q is the liquid flow rate. While changing the flow rate does not influence the evolution of the bubble neck diameter ($2r_0$), changing μ or d shifts the curves. (B) When time and length scales are nondimensionalized with the visco-capillary time scale $t^* = \mu d / \gamma$ and the tube diameter d , respectively, the data corresponding to all 12 experiments collapse onto a single curve ($\tilde{\tau} = \tau / t^* = \gamma \tau / (\mu d)$, and $\tilde{r}_0 = r_0 / d$). Here, two self-similar regimes can be observed: an early-time regime, which follows a $1/5$ power-law scaling in time, and a late-time regime very close to the point of pinch-off, which follows a linear scaling in time.

time (13, 38). Equating the two radial velocities corresponding to the early- and late-time regimes, we obtain an estimate of the cross-over time $\tau_c \sim t^* = \mu d / \gamma$, indicating that the visco-capillary time scale sets the point of transition between the two regimes. Fig. 2B shows that, indeed, using the visco-capillary time scale and the tube diameter as the characteristic time

and length scales leads to the collapse of all data corresponding to 12 different experiments with different tube diameters ($d = 280, 750 \mu\text{m}$), liquid viscosities ($\mu = 0.2, 1.4 \text{ Pa.s}$), and flow rates ($\text{Ca} = \mu U / \gamma \in [0.008, 0.02]$).

To test the self-similarity of the bubble neck profile, we probe its evolution in time in Fig. 3A (for the experiment with

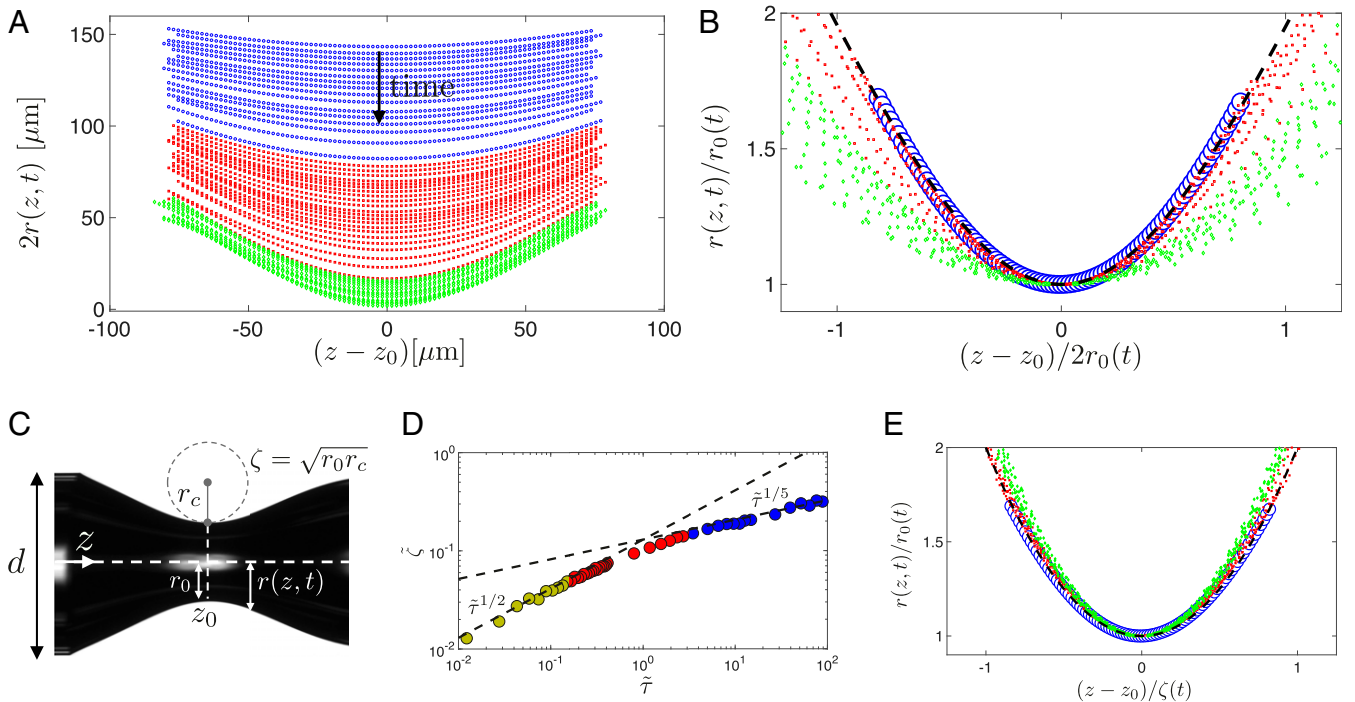


Fig. 3. Self-similarity of the neck profile. (A) The evolution of the bubble neck profile in time (data corresponding to $d = 750 \mu\text{m}$, $\mu = 1.4 \text{ Pa.s}$, and $\text{Ca} = 0.008$); blue and green symbols represent the data corresponding to the early and late-time self-similar regimes, and red symbols represent the transition between the two. (B) Scaling the neck profile with the minimum neck diameter collapses the data corresponding to the early-time self-similar regime, where $\tilde{R}(\xi) = \tilde{r}(\tilde{z}, \tilde{\tau}) / \tilde{\tau}^{1/5}$ and $\xi = (\tilde{z} - \tilde{z}_0) / \tilde{\tau}^{1/5}$. The dashed line, overlaying the blue symbols corresponding to the early-time self-similar regime, represents the self-similar solution of the long-wave model (SI Appendix, section 2). The data corresponding to the late-time self-similar regime, however, deviate from the predictions of the long-wave model. (C) The definition of parameters used to characterize the bubble neck profile. (D) The evolution of the axial length scale defined as $\tilde{\zeta} = \sqrt{r_0 r_c}$ versus time to pinch-off. In the early-time regime, $\tilde{\zeta} = \sqrt{r_0 r_c} \sim \tilde{\tau}^{1/5}$, consistent with the predictions of the long-wave model. In the late-time regime, however, $\tilde{r}_0 \sim \tilde{\tau}$ and $\tilde{\zeta} \sim \tilde{\tau}^{1/2}$, which indicates that the axial radius of curvature becomes constant, i.e., the neck profile becomes a parabola that simply translates in time (13, 42). (E) Scaling the axial length scale with the expressions obtained in D leads to the collapse of all bubble neck profiles during the entire pinch-off process (shown in A) onto a single parabolic curve: $r / r_0 = 1 + [(z - z_0) / \tilde{\zeta}]^2$ (dashed line).

$d = 750 \mu\text{m}$, $\mu = 1.4 \text{ Pa}\cdot\text{s}$, and $\text{Ca} = 0.008$), where the blue and green symbols correspond to the early- and late-time regimes, respectively, and red corresponds to the transition between the two regimes. The long-wave model predicts that the bubble neck diameter and also its axial extent both scale as $\tilde{\tau}^{1/5}$. In Fig. 3B, we show that, indeed, scaling both the neck diameter and axial dimension with the minimum neck diameter collapses the profiles in the early-time regime (blue symbols). The self-similar solution of the long-wave model Eq. 2 (black dashed line) fits the data in this regime. This observation further confirms the validity of the long-wave model in the early-time self-similar regime. The data in the late-time regime (green symbols), however, deviate from the predictions of the long-wave theory.

Very close to the point of pinch-off, in the late-time self-similar regime, we can simplify the balance of normal viscous stresses and the surface tension to obtain $\partial r / \partial \tau = \gamma / (2\mu)$ (13, 42). Assuming the scale invariance of the dynamics close to the singularity, and using the ansatz $\tilde{R}(\xi) = \tilde{r}(\tilde{z}, \tilde{\tau}) / \tilde{\tau}^\alpha$, and $\xi = (\tilde{z} - \tilde{z}_0) / \tilde{\tau}^\beta$, we obtain:

$$-\alpha \tilde{\tau}^{\alpha-1} \tilde{R} + \beta \tilde{\tau}^{\alpha-1} \xi \tilde{R}' = -1, \quad [3]$$

where the prime indicates differentiation with respect to ξ . For all of the terms to balance in time, we need to have $\alpha = 1$. The exponent β , however, remains undetermined; this is one of the hallmarks of self-similarity of the second kind (39). The value of the exponent β can be obtained from matching the solution close to the pinch-off to the outer solution and imposing the regularity and stability of the solution (43). This leads to an eigenvalue problem, the solution of which shows that $\beta = 1/2$ (SI Appendix, section 4).

In the local neighborhood of the minimum neck radius, we expect the profile to be parabolic: $r(z, t) = r_0(t) + (z - z_0)^2 / r_c(t)$, where r_0 is the minimum neck radius, and r_c is the axial radius of curvature. Scaling the profile with the radius $r_0(t)$, we then obtain $r/r_0 = 1 + (z - z_0)^2 / \zeta^2$, where $\zeta = \sqrt{r_c r_0}$ represents the axial extent of the parabola. We fit a parabola to the neck profile in the vicinity of the minimum neck radius to extract the axial length scale ζ . In the early-time self-similar regime, the long-wave model predicted that $\zeta \sim \tilde{\tau}^{1/5}$. In the late-time self-similar regime, we further showed that Eq. 3 indicates the axial extent of the profile scales as $\zeta \sim \tilde{\tau}^{1/2}$. Both of these detailed predictions are supported by the experimental data in

Fig. 3D. Using ζ as the axial length scale, we can therefore collapse the neck profiles over the entire pinch-off process onto a single parabolic curve (Fig. 3E).

In the early-time self-similar regime, both the neck radius, $r_0(\tau)$, and the corresponding axial radius of curvature, $r_c(\tau)$, are time-dependent. However, in the late-time regime, we have $\tilde{r}_0 \sim \tilde{\tau}$ (Fig. 2B), and the axial scale of the profile scale as $\tilde{\zeta} = \sqrt{\tilde{r}_c \tilde{r}_0} \sim \tilde{\tau}^{1/2}$ (Fig. 3C), indicating that the axial radius of curvature of the neck profile becomes independent of time: $r_{cf} \equiv \lim_{\tilde{\tau} \rightarrow 0} r_c(\tau) = \text{constant}$. The temporal invariance of the axial radius of curvature of the bubble neck might suggest that the separation of scales is lost and the singularity formation becomes nonuniversal. In other words, the axial extent of the neck profile retains an imprint of the details of the experimental system, and the memory of the initial conditions will persist all of the way to the point of pinch-off (13, 42).

In our system, however, this late-time self-similar regime is preceded by an early-time self-similar regime of the first kind, which sets the axial length scale of the late-time regime at the cross-over between the two regimes. This characterization is captured in Fig. 3D, which shows a cross-over in the scaling of the axial length scale at $\tilde{\tau} \approx 1$ (see also SI Appendix, section 5). In the early-time regime, we have $\tilde{r}_0 \approx 0.09 \tilde{\tau}^{1/5}$, and $\tilde{r}_c \approx 0.19 \tilde{\tau}^{1/5}$, leading to $\tilde{\zeta} = \sqrt{\tilde{r}_c \tilde{r}_0} \approx 0.13 \tilde{\tau}^{1/5}$ as the scaling of the axial length scale. In the late-time regime, we also have $\tilde{\zeta} = \sqrt{\tilde{r}_c \tilde{r}_0} \approx 0.5 \tilde{\tau}^{1/2} \sqrt{\tilde{r}_{cf}}$. Therefore, at the point of cross-over, $\tilde{\tau} \approx 1$, the early-time self-similar regime sets the axial length scale of the late-time regime ($\tilde{\zeta} \approx 0.13$), leading to $\tilde{r}_{cf} \approx 0.07$. Fig. 4A shows a plot of the axial radius of curvature as a function of time to the pinch-off for each experiment. When nondimensionalized, we observe that, indeed, the data corresponding to all 12 experiments collapse onto a single curve (Fig. 4B), with an asymptotic universal radius of curvature of $\tilde{r}_{cf} \approx 0.07$. This observation indicates that the early-time self-similar regime effectively erases the system's memory of the initial conditions and restores universality to bubble pinch-off in a viscous liquid.

We therefore conclude that the combined effect of geometric confinement and contact-line motion leads to the emergence of an early-time self-similar regime of the first kind, which at late times crosses over to a regime of self-similarity of the second kind. While the balance between viscous and capillary forces controls the dynamics of interface evolution in both regimes, the cross-over occurs due to a change in the dominant contribution to the viscous dissipation; from the spatially localized moving

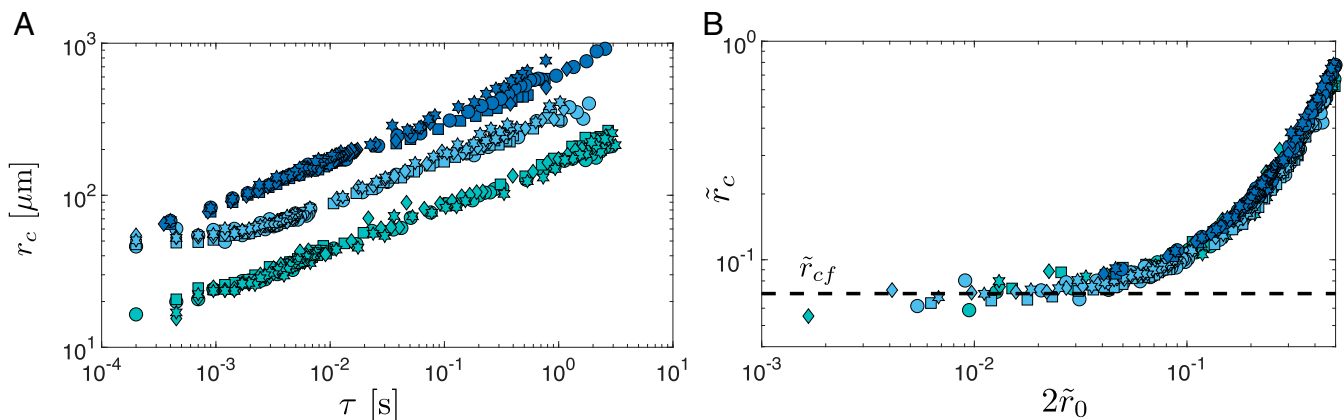


Fig. 4. Axial radius of curvature versus time. The evolution of the axial radius of curvature r_c versus time to the pinch-off shows that as the point of pinch-off is approached, the curvature asymptotes to a constant value (symbols are the same as in Fig. 2). (A) The time evolution of axial radius of curvature is independent of the flow rate but changes when the liquid viscosity or the tube diameter is varied. (B) The data corresponding to all 12 experiments collapse on a single curve when the nondimensional axial radius of curvature is plotted against the nondimensional minimum neck diameter. The nondimensional late-time axial radius of curvature asymptotes to a universal constant $\lim_{\tilde{\tau} \rightarrow 0} \tilde{r}_c(\tilde{\tau}) = \tilde{r}_{cf} \approx 0.07$.

contact-line singularity at early times to the temporally localized bubble pinch-off singularity at late times. This change in the dominant contributor to the viscous effects is accompanied by a change in the direction of the flow, from axially dominated in the early-time regime to radially dominated in the late-time regime. The late-time regime is also observed in the pinch-off of bubbles in unbounded fluid domains, where the flow is mainly radial and the axial length scale characterizing the bubble neck is sensitive to the details of the experimental system, making the pinch-off nonuniversal (13, 34–36). Here, in the case of bubble pinch-off in confined domains, however, we observe that the axial length scale of the neck region is set by the early-time self-similar regime, effectively erasing the system's memory of the initial conditions and restoring universality to the pinch-off process.

While we have focused on the case of bubble pinch-off in a viscous liquid, we expect our observation of the universality of the

pinch-off process to persist for any other (at least viscously dominated) fluid–fluid displacement process in a confined medium involving moving contact lines. The restoration of universality has important consequences for controlled generation of bubbles, drops, and emulsions in microfluidic devices with a myriad of applications in medicine (44, 45) and material science (46–50), as well as for understanding of multiphase flows in geologic media (22, 51), where geometric confinement and liquid–solid physicochemical interactions play a key role.

Materials and Methods

Materials and Methods are described in [SI Appendix](#).

ACKNOWLEDGMENTS. We thank Denis Bartolo and Jens Eggers for insightful discussions, and Benzhong Zhao for advice on the experimental setup. This work was funded by the US Department of Energy (Grant no. DE-SC0018357).

1. F. Savart, *Mémoire sur le choc d'une veine liquide lancée contre un plan circulaire* [in French]. *Ann. Chim.* **53**, 337–398 (1833).
2. J. Plateau, *Recherches expérimentales et théorique sur les figures d'équilibre d'une masse liquide sans pesanteur* [in French]. *Acad. Sci. Brux. Mem.* **23**, 5 (1849).
3. L. Rayleigh, On the instability of jets. *Proc. Lond. Math. Soc.* **s1-10**, 4–13 (1879).
4. L. Rayleigh, Some applications of photography. *Nature* **44**, 249–254 (1891).
5. A. M. Worthington, *A Study of Splashes* (Longmans, London, UK, 1908).
6. H. E. Edgerton, E. A. Hauser, W. B. Tucker, Studies in drop formation as revealed by the high-speed motion camera. *J. Phys. Chem.* **41**, 1017–1028 (1937).
7. X. D. Shi, M. P. Brenner, S. R. Nagel, A cascade of structure in a drop falling from a faucet. *Science* **265**, 219–222 (1994).
8. S. T. Thoroddsen, T. G. Etoh, K. Takehara, High-speed imaging of drops and bubbles. *Annu. Rev. Fluid Mech.* **40**, 257–285 (2008).
9. J. Eggers, Nonlinear dynamics and breakup of free-surface flows. *Rev. Mod. Phys.* **69**, 865–930 (1997).
10. J. Eggers, Universal pinching of 3D axisymmetric free-surface flow. *Phys. Rev. Lett.* **71**, 3458–3460 (1993).
11. J. R. Lister, H. A. Stone, Capillary breakup of a viscous thread surrounded by another viscous fluid. *Phys. Fluids* **10**, 2758–2764 (1998).
12. I. Cohen, M. P. Brenner, J. Eggers, S. R. Nagel, Two fluid drop snap-off problem: Experiments and theory. *Phys. Rev. Lett.* **83**, 1147–1150 (1999).
13. P. Doshi *et al.*, Persistence of memory in drop breakup: The breakdown of universality. *Science* **302**, 1185–1188 (2003).
14. R. Bergmann *et al.*, Giant bubble pinch-off. *Phys. Rev. Lett.* **96**, 154505 (2006).
15. J. Eggers, M. A. Fontelos, D. Leppinen, J. H. Snoeijer, Theory of the collapsing axisymmetric cavity. *Phys. Rev. Lett.* **98**, 094502 (2007).
16. S. Gekle, A. van der Bos, R. Bergmann, D. van der Meer, D. Lohse, Noncontinuous Froude number scaling for the closure depth of a cylindrical cavity. *Phys. Rev. Lett.* **100**, 084502 (2008).
17. L. E. Schmidt, N. C. Keim, W. W. Zhang, S. R. Nagel, Memory-encoding vibrations in a disconnecting air bubble. *Nat. Phys.* **5**, 343–346 (2009).
18. H. A. Stone, A. D. Stroock, A. Ajdari, Engineering flows in small devices: Microfluidics toward a lab-on-a-chip. *Annu. Rev. Fluid Mech.* **36**, 381–411 (2004).
19. A. S. Utada *et al.*, Monodisperse double emulsions generated from a microcapillary device. *Science* **308**, 537–541 (2005).
20. A. M. Gañán-Calvo, R. González-Prieto, P. Riesco-Chueca, M. A. Herrada, M. Flores-Mosquera, Focusing capillary jets close to the continuum limit. *Nat. Phys.* **3**, 737–742 (2007).
21. M. J. Fuerstman, P. Garstecki, G. M. Whitesides, Coding/decoding and reversibility of droplet trains in microfluidic networks. *Science* **315**, 828–832 (2007).
22. A. Parmigiani, S. Faroughi, C. Huber, O. Bachmann, Y. Su, Bubble accumulation and its role in the evolution of magma reservoirs in the upper crust. *Nature* **532**, 492–495 (2016).
23. S. L. Anna, Droplets and bubbles in microfluidic devices. *Annu. Rev. Fluid Mech.* **48**, 285–309 (2016).
24. P. Garstecki, H. A. Stone, G. M. Whitesides, Mechanism for flow-rate controlled breakup in confined geometries: A route to monodisperse emulsions. *Phys. Rev. Lett.* **94**, 164501 (2005).
25. J. C. Burton, P. Taborek, Role of dimensionality and axisymmetry in fluid pinch-off and coalescence. *Phys. Rev. Lett.* **98**, 224502 (2007).
26. B. Dollet, W. van Hoeve, J. P. Raven, P. Marmottant, M. Versluis, Role of the channel geometry on the bubble pinch-off in flow-focusing devices. *Phys. Rev. Lett.* **100**, 034504 (2008).
27. V. van Steijn, C. R. Kleijn, M. T. Kreutzer, Flows around confined bubbles and their importance in triggering pinch-off. *Phys. Rev. Lett.* **103**, 214501 (2009).
28. M. Yokota, K. Okumura, Dimensional crossover in the coalescence dynamics of viscous drops confined in between two plates. *Proc. Natl. Acad. Sci. U.S.A.* **108**, 6395–6398 (2011).
29. P. G. de Gennes, Wetting: Statics and dynamics. *Rev. Mod. Phys.* **57**, 827–863 (1985).
30. C. Huh, L. Scriven, Hydrodynamic model of steady movement of a solid/liquid/fluid contact line. *J. Colloid Interf. Sci.* **35**, 85–101 (1971).
31. D. Bonn, J. Eggers, J. Indekeu, J. Meunier, E. Rolley, Wetting and spreading. *Rev. Mod. Phys.* **81**, 739–805 (2009).
32. G. H. McKinley, Visco-elasto-capillary thinning and break-up of complex fluids. *Rheol. Rev.* **3**, 1–48 (2005).
33. J. R. Castrejón-Pita *et al.*, Plethora of transitions during breakup of liquid filaments. *Proc. Natl. Acad. Sci. U.S.A.* **112**, 4582–4587 (2015).
34. R. Suryo, P. Doshi, O. A. Basaran, Non-self-similar, linear dynamics during pinch-off of a hollow annular jet. *Phys. Fluids* **16**, 4177–4184 (2004).
35. S. T. Thoroddsen, T. G. Etoh, K. Takehara, Experiments on bubble pinch-off. *Phys. Fluids* **19**, 042101 (2007).
36. J. Eggers, E. Villermaux, Physics of liquid jets. *Rep. Prog. Phys.* **71**, 036601 (2008).
37. B. Zhao, A. A. Pahlavan, L. Cueto-Felgueroso, R. Juanes, Forced wetting transition and bubble pinch-off in a capillary tube. *Phys. Rev. Lett.* **120**, 084501 (2018).
38. J. C. Burton, R. Waldrep, P. Taborek, Scaling and instabilities in bubble pinch-off. *Phys. Rev. Lett.* **94**, 184502 (2005).
39. G. I. Barenblatt, *Scaling, Self-Similarity, and Intermediate Asymptotics: Dimensional Analysis and Intermediate Asymptotics* (Cambridge Univ Press, Cambridge, UK, 1996).
40. C. Redon, F. Brochard-Wyart, F. Rondelez, Dynamics of dewetting. *Phys. Rev. Lett.* **66**, 715–718 (1991).
41. J. H. Snoeijer, J. Eggers, Asymptotic analysis of the dewetting rim. *Phys. Rev. E* **82**, 056314 (2010).
42. J. Eggers, M. A. Fontelos, *Singularities: Formation, Structure, and Propagation* (Cambridge Univ Press, Cambridge, UK, 2015).
43. J. Eggers, “Singularities at interfaces” in *Soft Interfaces*, L. Bocquet, D. Quéré, T. A. Witten, L. F. Cugliandolo, Eds. (Lecture Notes of the Les Houches Summer School, Oxford Univ Press, Oxford, UK, 2012), vol. **98**, pp. 101–132.
44. J. R. Lindner, Microbubbles in medical imaging: Current applications and future directions. *Nat. Rev. Drug Discov.* **3**, 527–533 (2004).
45. J. Rodríguez-Rodríguez, A. Sevilla, C. Martínez-Bazán, J. M. Gordillo, Generation of microbubbles with applications to industry and medicine. *Annu. Rev. Fluid Mech.* **47**, 405–429 (2015).
46. P. C. Huzyak, K. W. Koelling, The penetration of a long bubble through a viscoelastic fluid in a tube. *J. Non-Newtonian Fluid Mech.* **71**, 73–88 (1997).
47. O. A. Basaran, Small-scale free surface flows with breakup: Drop formation and emerging applications. *AIChE J.* **48**, 1842–1848 (2002).
48. H. Wijshoff, The dynamics of the piezo inkjet printhead operation. *Phys. Rep.* **491**, 77–177 (2010).
49. J. I. Park, A. Saffari, S. Kumar, A. Günther, E. Kumacheva, Microfluidic synthesis of polymer and inorganic particulate materials. *Annu. Rev. Mater. Res.* **40**, 415–443 (2010).
50. E. Amstad *et al.*, Production of amorphous nanoparticles by supersonic spray-drying with a microfluidic nebulator. *Science* **349**, 956–960 (2015).
51. M. L. Szulczewski, C. W. MacMinn, H. J. Herzog, R. Juanes, Lifetime of carbon capture and storage as a climate-change mitigation technology. *Proc. Natl. Acad. Sci. U.S.A.* **109**, 5185–5189 (2012).

Supplementary Materials for
Restoring universality to the pinch-off of a bubble

Amir A. Pahlavan,^{1,2} Howard A. Stone,² Gareth H. McKinley,¹ and Ruben Juanes¹

¹*Massachusetts Institute of Technology, Cambridge, Massachusetts, USA*

²*Department of Mechanical and Aerospace Engineering,
Princeton University, Princeton, New Jersey, USA**

(Dated:)

* pahlavan@princeton.edu

This PDF file includes:

1. Materials and Methods
2. Supplementary Text
3. Figs. S1 and S2
4. Captions for Movies S1 and S2

I. MATERIALS AND METHODS

We use precision-made borosilicate glass capillary tubes with two different inner diameters ($d = 280, 750 \mu\text{m}$). We wash the capillary tubes with isopropyl alcohol and ethanol, followed by an ultrasonic cleaning step in a de-ionized water bath for one hour. The capillary tubes are then dried using compressed nitrogen gas. We use glycerol (viscosity $\mu = 1.4 \text{ Pa.s}$) and 90% glycerol-water mixture (viscosity $\mu = 0.2 \text{ Pa.s}$) as the liquid phase. Both liquids are partially wetting to the tube with a contact angle of ≈ 25 degrees. The receding contact line speed is proportional to the equilibrium contact angle cubed ($\sim \theta_{eq}^3$) [1, 2]; therefore, to accelerate the pinch-off process, we make the tubes less wetting to the liquid through heat-assisted chemical vapor deposition step of trichloro(1H,1H,2H,2H-perfluorooctyl)silane (Sigma-Aldrich, USA) in a vacuum oven, which leads to a contact angle of $\approx 65^\circ$.

The capillary tube is open to the atmosphere at the left end and is connected to a syringe pump at the right end. The tube is initially filled with glycerol and then the glycerol is withdrawn at a specified flow rate Q from the right end of the tube using a syringe pump (CETONI low pressure pump neMESYS), leading to the air penetrating the tube from the left side. To achieve refractive-index matching and an undistorted view of the displacement process, we house the circular capillary tube inside a square tube (both tubes are made of borosilicate glass) and fill the gap between the two with glycerol. When the capillary tube is filled with glycerol, light goes through the system without any refraction (white color in Fig. 1 of the main text). When air penetrates the tube, it leads to the refraction of light to the center of the tube; therefore air appears in black color with a straight white line in the middle. The capillary tube is backlit with a LED light source (120E, Veritas). Imaging is done from the front side using a high-speed camera (Phantom Micro 320) at a typical frame-rate of 10–25 kfps. A 4X lens is mounted on the camera leading to a resolution of $1.7 \mu\text{m}/\text{pixel}$.

II. LONG-WAVE MODEL FOR THE DEWETTING RIM

When glycerol is withdrawn from the tube at a high-enough flow rate ($Q > Q_c$) [2], air penetrates the tube from the left side leaving a film of the liquid on the walls. Since the liquid is partially wetting to the tube ($\theta_{eq} \approx 65^\circ$) it starts dewetting from the tube wall, forming a growing dewetting rim (Fig. 1). Initially, the flow in the film is mainly due to the receding of the contact line, leading to the flow to be mainly parallel to the tube axis. This observation allows us to describe the dynamics of the growing dewetting rim using a long-wave approximation [2]:

$$\frac{\partial \tilde{r}}{\partial \tilde{\tau}} = \frac{1}{(16)^2} \frac{1}{\tilde{r}} \frac{\partial}{\partial \tilde{z}} \left(\mathcal{M}(\tilde{r}) \frac{\partial}{\partial \tilde{z}} [\Pi(\tilde{r}) - \tilde{\kappa}] \right), \quad (1)$$

where $\tilde{r}(\tilde{z}, \tilde{\tau})$ is the radius of bubble neck, $\mathcal{M}(\tilde{r}) = 1 - 16\tilde{r}^2 + 48\tilde{r}^4 - 64\tilde{r}^4 \ln 2\tilde{r}$ is the mobility, $\Pi(\tilde{r}) = 6(1 - \cos \theta_{eq})(\delta^2/(1/2 - \tilde{r})^3)(1 - \delta/(1/2 - \tilde{r}))$ is the disjoining pressure with δ as the precursor film thickness, and $\tilde{\kappa} = 1/\tilde{r} - \tilde{r}_{\tilde{z}\tilde{z}}$ is the curvature. Here, all length scales are non-dimensionalized by the tube diameter d , and the dimensionless time to the pinch-off is defined as $\tilde{\tau} = \tau/t^*$, where $\tau = (t_0 - t)$ is the time to the pinch-off with t_0 as the breakup time and $t^* = \mu d/\gamma$ is the visco-capillary time scale.

Near the point of pinch-off, we postulate that the shape of the profile becomes self-similar: $\tilde{R}(\xi) = \tilde{r}(\tilde{z}, \tilde{\tau})/\tilde{\tau}^\alpha$, and $\xi = (\tilde{z} - \tilde{z}_0)/\tilde{\tau}^\beta$. We can neglect the disjoining pressure in the vicinity of the singularity, which is far away from the contact line. Substituting this ansatz back into Eq. (1), we recover Eq. (1) of the main text:

$$(-\alpha \tilde{R} + \beta \xi \tilde{R}') \tilde{\tau}^{\alpha-1} = \frac{1}{(16)^2} \frac{1}{\tilde{R}} \left(\left[-\frac{2}{\tilde{R}^3} \tilde{R}'^2 + \frac{1}{\tilde{R}^2} \tilde{R}'' \right] \tilde{\tau}^{-2(\alpha+\beta)} + \tilde{R}'''' \tilde{\tau}^{-4\beta} \right), \quad (2)$$

where prime indicates differentiation. For all the terms to balance in time we need to have $\alpha = \beta = 1/5$, which leads to $\tilde{R}(\xi) = \tilde{r}(\tilde{z}, \tilde{\tau})/\tilde{\tau}^{1/5}$, and $\xi = (\tilde{z} - \tilde{z}_0)/\tilde{\tau}^{1/5}$. The equation governing the dewetting rim in the early self-similar regime is therefore the following:

$$(-\tilde{R} + \xi \tilde{R}') = \frac{5}{(16)^2} \frac{1}{\tilde{R}} \left(\left[-\frac{2}{\tilde{R}^3} \tilde{R}'^2 + \frac{1}{\tilde{R}^2} \tilde{R}'' \right] + \tilde{R}'''' \right), \quad (3)$$

which represents the balance of viscous forces on the left-hand side with the surface tension forces on the right-hand side.

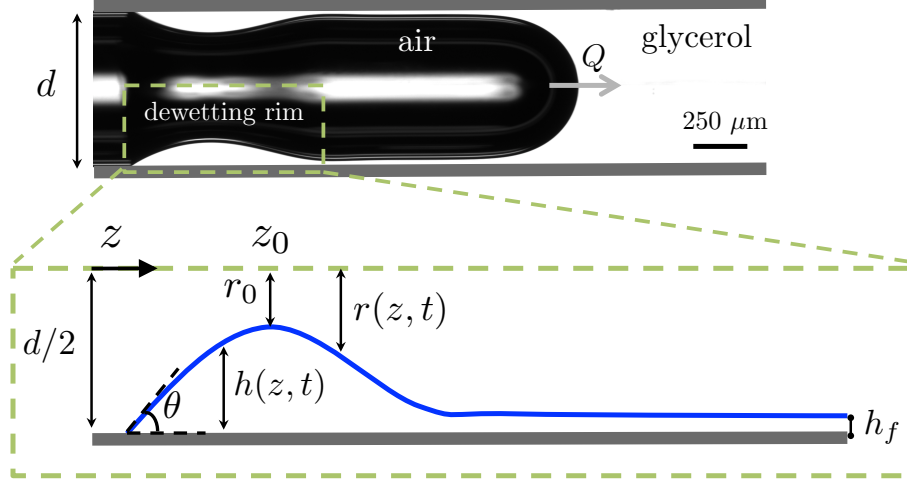


FIG. 1. Schematics of the dewetting rim: as the contact line recedes from the tube wall, liquid accumulates behind it and the rim keeps growing. The dynamics of this growing rim can be described using a long-wave approximation (Eq. (1)). The film thickness downstream of the rim is set by the Taylor–Bretherton scaling $h_f/(d/2) = 1.34\text{Ca}_f^{2/3}/(1 + 1.34 \times 2.5\text{Ca}_f^{2/3})$, where $\text{Ca}_f = \mu U_f/\gamma$ with U_f as the air finger velocity[3–6]. This relationship combined with the conservation of mass: $Q = \pi(d/2 - h_f)^2 U_f$ determine both the finger velocity and the film thickness.

This type of ordinary differential equations typically leads to an infinite family of solutions, where only one is found to be stable [7, 8]. To obtain the self-similar solution of the ODE, we solve the original partial differential equation (1) numerically and extract the self-similar solution from the late-time solution of the PDE very close to the point of pinch-off. The self-similar solution obtained using this technique is shown as the dashed line in Fig. 3(b) of the main text, and shows an excellent agreement with the experimental data at the early-time self-similar regime, where the long-wave model is valid.

III. CROSSOVER TIME

To estimate the crossover time between the two regimes, we compare their corresponding radial velocities. In the early-time regime, the growth rate of the dewetting rim is proportional to the velocity of the receding contact line, i.e. $dr_0/d\tau \sim u_{cl} \sim (\gamma/\mu)\theta_{eq}^3$, which is nearly constant for a given wettability [1, 2]. In the late-time regime, the bubble neck close to the point of singularity can be approximated as an axisymmetric cylinder, and the flow in the viscous fluid can be approximated as radial. The normal viscous stress generated by the radial flow is balanced by surface tension, leading to $dr_0/dt = -\gamma/(2\mu)(1 - 2r_0/r_c)$ [9], where $r_c \approx r_c(t = 0)$ is the axial radius of curvature. The radius of the neck can therefore be approximated as $r_0(t) = r_{00}[1 - r_c/(2r_{00})]e^{\gamma t/(\mu r_c)} + r_c/(2r_{00})$ where $r_{00} = r_0(t = 0)$, leading to $dr_0/d\tau \sim (\gamma/\mu)e^{-\tau/t^*}$ as the radial velocity in the late-time regime [9]. Note that very close to the point of pinch-off, we have $r_0 \ll r_c$, leading to $dr_0/d\tau = \gamma/(2\mu)$, which is the familiar linear scaling in time [10]. Equating the two radial velocities corresponding to the early and late-time regimes we obtain an estimate of the crossover time $\tau_c \sim t^* = \mu d/\gamma$, indicating that the visco-capillary time scale sets the point of transition between the two regimes.

IV. SELF-SIMILARITY OF THE BUBBLE NECK IN A LARGE QUIESCENT TANK

Here, we briefly review how to determine the value of the exponent β in the second self-similar regime [11]. In the late-time self-similar regime, we can approximate the bubble neck as a cylinder, which effectively acts as a sink sucking the liquid radially towards the tube center. The normal viscous stress jump across the air-liquid cylindrical interface is balanced by the surface tension, leading to $\partial r / \partial t = -\gamma / (2\mu)$. Therefore, the neck profile is simply translated in time without changing its shape. We postulate the neck profile becomes self-similar, following a scaling ansatz $\tilde{R}(\xi) = \tilde{r}(\tilde{z}, \tilde{\tau}) / \tilde{\tau}^\alpha$, and $\xi = (\tilde{z} - \tilde{z}_0) / \tilde{\tau}^\beta$. Substituting this ansatz back into the governing equation for the neck profile, we obtain:

$$-\alpha \tilde{\tau}^{\alpha-1} \tilde{R} + \beta \tilde{\tau}^{\alpha-1} \xi \tilde{R}' = -1, \quad (4)$$

where prime indicates differentiation. For all the terms to balance in time we need to have $\alpha = 1$. The value of the exponent β , however, cannot be determined from dimensional analysis, indicating that the self-similarity is of the second kind [12].

The solution of Eq. (4) is described by $\tilde{R} = 1 + a \tilde{\xi}^{1/\beta}$, in which a is a constant of integration that depends on the outer solution away from the singularity. Close to the pinch-off time, the neck profile away from the singularity becomes effectively frozen in time, which leads to a constraint on the behavior of the self-similar solution: $\tilde{r}(\tilde{z} \rightarrow \tilde{z}_0 \pm \epsilon, \tilde{\tau} \rightarrow \epsilon) = \tilde{\tau}^\alpha \tilde{R}((\tilde{z} - \tilde{z}_0) / \tilde{\tau}^\beta) = \text{const}$, and therefore we need to have $\tilde{R}(\xi \rightarrow \pm\infty) \sim \xi^{\alpha/\beta}$. The regularity condition also implies that $1/\beta$ must be a positive even integer, and $a > 0$. We can therefore have a discrete family of solutions for β , i.e. $\beta_i = 1/(2i)$ with $i = 1, 2, \dots$. This is similar to the breakup of a drop, where also an infinite family of solutions is obtained [7, 8].

To find out which one of these solutions is selected, we need to address the stability of these solutions. Briefly, we use a change of variables $T = -\ln \tilde{\tau}$, rewriting the equation governing the self-similar profile as $R_T = R - \beta \xi R' - 1$, which is a dynamical system representation of the original equation, for which the original self-similar solution will be a fixed point. We can therefore perturb the self-similar solution as $\tilde{R}(\xi, T) = \bar{R}(\xi) + \epsilon e^{nT} P(\xi)$, where n is the eigenvalue and P is the eigenfunction. The stability analysis [11] shows that the stable solution is

described by $\beta = 1/2$, i.e. $\tilde{R}(\xi) = 1 + a\xi^2$. This implies that the neck profile can be described as $\tilde{r}(\tilde{z}, \tilde{\tau}) = \tilde{\tau}(1 + a[(\tilde{z} - \tilde{z}_0)/\tilde{\tau}^{1/2}]^2) = \tilde{\tau} + a(\tilde{z} - \tilde{z}_0)^2$, which is a parabola that is simply translated in time.

V. EVOLUTION OF THE LATERAL LENGTH SCALE IN TIME

In Fig. 3 of the main text, we showed that using the lateral length scale $\zeta = \sqrt{r_0 r_c}$ extracted from the experimental data ($d = 750 \mu\text{m}$, $\mu = 1.4 \text{ Pa.s}$, and $\text{Ca} = 0.008$), we can collapse the neck profiles during its entire time evolution onto a single parabola. To extract the axial length scale ζ , we fit a parabola to the neck profile in the vicinity of the minimum neck radius. Another technique recently developed by Wagoner et al. [13] extracts the axial length scale of the neck from the calculation of the pinch-off zone volume. The pinch-off zone is defined as the region between the minimum neck radius, r_0 , and $r = \alpha r_0$ with $1 < \alpha < 2$. Fig. 2 shows that the neck volume at early times follows the scaling $\tilde{\tau}^{3/5}$ and at late times follows the scaling $\tilde{\tau}^{5/2}$. The neck volume scales as $r_0^2 \zeta$, and we know that $\tilde{r}_0 \sim \tilde{\tau}^{1/5}$ at early times and $\tilde{r}_0 \sim \tilde{\tau}$ at late times. Therefore, the evolution of the neck volume in time indicates that $\tilde{\zeta} \sim \tilde{\tau}^{1/5}$ at early times and $\tilde{\zeta} \sim \tilde{\tau}^{1/2}$ at late times. Therefore, calculating the axial length scale using the new technique further confirms our results.

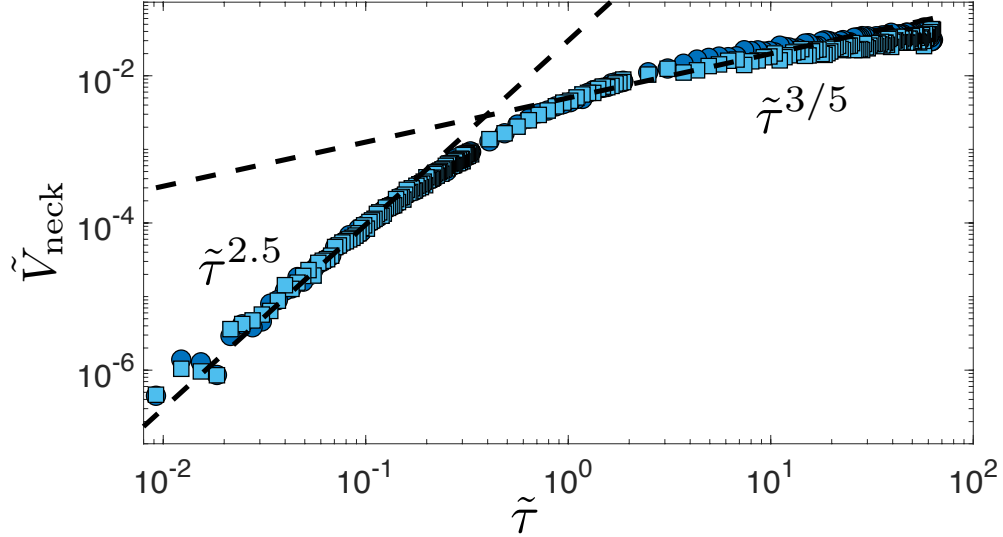


FIG. 2. The evolution of the volume of the pinching zone as a function of time to the pinch off, showing two distinct scalings in time at early and late time regimes. The squares and circles represent the neck half volume to the left and right of the minimum neck radius. Here, we have taken the pinch-off zone to be the region between the minimum neck radius, r_0 , and $r = \alpha r_0$ with $\alpha = 1.3$. We have further confirmed that the scalings are insensitive to the value of α by repeating this procedure in the range $1.1 < \alpha < 1.7$.

In Fig. 3 we present the lateral length scale evolution data corresponding to all the 12 experiments. We find that, indeed, scaling the lateral length scale with the tube diameter and the time scale with the visco-capillary time collapses the data corresponding to all the experiments. The scaling of $\tilde{\zeta} = \sqrt{\tilde{r}_c \tilde{r}_0} \sim \tilde{\tau}^{1/2}$ in the late-time regime indicates that the axial radius of curvature in the second regime becomes time-independent. The asymptotic value of the axial curvature is therefore set by the first self-similar regime at the point of crossover between the two regimes, where $\tilde{\zeta} \approx 0.13$, leading to $\tilde{r}_{cf} \equiv \tilde{r}_c(\tilde{\tau} \rightarrow 0) \approx 0.07$, making this asymptotic curvature universal, in contrast to the non-universal case of bubble breakup in an unbounded reservoir [10].

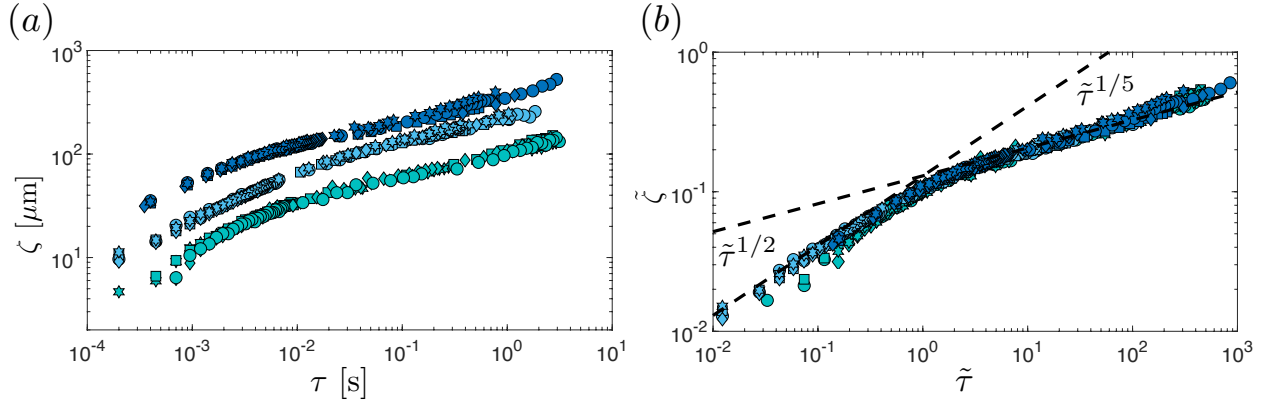


FIG. 3. The evolution of the lateral length scale of the bubble neck ($\zeta = \sqrt{r_0 r_c}$) in time: (a) dimensional, and (b) non-dimensional. Data from 12 different experiments are shown: light blue symbols correspond to $d = 750 \mu\text{m}$ and $\mu = 1.4 \text{ Pa.s}$; the cyan symbols correspond to $d = 280 \mu\text{m}$ and $\mu = 1.4 \text{ Pa.s}$; the dark blue symbols correspond to $d = 750 \mu\text{m}$ and $\mu = 0.2 \text{ Pa.s}$. Each color represents data corresponding to 4 different flow rates with $\text{Ca} = \mu U / \gamma \in [0.008, 0.02]$, where $U = 4Q / (\pi d^2)$ and Q is the liquid flow rate. While changing the flow rate does not influence the evolution of the lateral length scale ($\tilde{\zeta}$), changing μ or d shifts the curves.

VI. CAPTIONS OF SUPPLEMENTARY MOVIES

- **Movie S1:** Evolution of the dewetting rim and the ultimate breakup of the bubble in a capillary tube with the diameter $d = 280 \mu\text{m}$, and $\text{Ca} = 0.016$. The imaging is done at 20 kfps.
- **Movie S2:** Motion of a microbubble in the vicinity of the bubble neck. The microbubble here acts as a tracer, showing the flow direction, which is axially-dominant at early times and crosses over to a radially-dominant flow at late times.

-
- [1] J. H. Snoeijer and J. Eggers. Asymptotic analysis of the dewetting rim. *Phys. Rev. E*, 82:056314, 2010.
- [2] B. Zhao, A. A. Pahlavan, L. Cueto-Felgueroso, and R. Juanes. Forced wetting transition and bubble pinch-off in a capillary tube. *Phys. Rev. Lett.*, 120:084501, 2018.
- [3] G. I. Taylor. Deposition of a viscous fluid on the wall of a tube. *Journal of Fluid Mechanics*, 10(2):161–165, 1961.
- [4] F. P. Bretherton. The motion of long bubbles in tubes. *Journal of Fluid Mechanics*, 10(2):166–188, 1961.
- [5] P. Aussillous and D. Quéré. Quick deposition of a fluid on the wall of a tube. *Physics of Fluids*, 12(10):2367–2371, 2000.
- [6] E. Klaseboer, R. Gupta, and R. Manica. An extended bretherton model for long taylor bubbles at moderate capillary numbers. *Physics of Fluids*, 26(3):032107, 2014.
- [7] D. T. Papageorgiou. On the breakup of viscous liquid threads. *Physics of Fluids*, 7(7):1529–1544, 1995.
- [8] M. P. Brenner, J. R. Lister, and H. A. Stone. Pinching threads, singularities and the number 0.0304... *Physics of Fluids*, 8(11):2827–2836, 1996.
- [9] R. Bolaños-Jiménez, A. Sevilla, C. Martínez-Bazán, D. van der Meer, and J. M. Gordillo. The effect of liquid viscosity on bubble pinch-off. *Physics of Fluids*, 21(7):072103, 2009.
- [10] P. Doshi, I. Cohen, W. W. Zhang, M. Siegel, P. Howell, O. A. Basaran, and S. R. Nagel. Persistence of memory in drop breakup: The breakdown of universality. *Science*, 302(5648):1185–1188, 2003.
- [11] J. Eggers. *Singularities at Interfaces*, volume 98 of *Lecture Notes of the Les Houches Summer School*, pages 101–132. Oxford University Press, 2012.
- [12] G. I. Barenblatt. *Scaling, Self-similarity, and Intermediate Asymptotics: Dimensional Analysis and Intermediate Asymptotics*. Cambridge University Press, 1996.
- [13] B. W. Wagoner, S. S. Thete, and O. A. Basaran. A new experimental method based on volume measurement for determining axial scaling during breakup of drops and liquid threads. *Physics of Fluids*, 30(8):082102, 2018.

In this issue ...

Snail-inspired superglue

Commercial adhesives are either strong and irreversible, such as superglues, or weak and reusable, such as pressure-sensitive tapes. Some biologically inspired adhesives such as Velcro are both strong and reversible, but they require interlocking structures on opposing surfaces for adhesion. To create a strong and reversible adhesive that works on an array of surfaces, Hyesung Cho,



Land snail adhering to a rough surface using its epiphragm. Image courtesy of Younghee Lee (photographer).

Gaoxiang Wu, Jason Christopher Jolly, et al. (pp. 13774–13779) fashioned a hydrogel that combines the desirable properties of liquid and dry adhesives, drawing inspiration from snails. Snails glide along rough and uneven surfaces, secreting mucus, which provides traction. As the mucus dries and hardens, its shear modulus rises from 100 Pa to 1 GPa, resulting in a structure called an epiphragm, which cements the snail to the surface. The authors developed a reversible hydrogel made of poly(2-hydroxyethyl methacrylate) (PHEMA) that works on smooth and rough surfaces, with adhesive strengths reaching 892 N/cm², comparable to superglues. Like the snail's epiphragm, the gel deforms in its soft, wet state to adapt and adhere to the target surface. Upon drying, the gel shrinks, turns glassy, and interlocks with the surface, its shear modulus increasing by 3 orders of magnitude to around 2.3 GPa. Rehydrating the gel liberates the stored energy, restores the gel's original shape, and quickens detachment—a physical attribute termed shape adaptation and memory. The authors scaled up the adhesive by layering the hydrogel atop a silicon backbone attached to a tendon made of Kevlar tape. Using only a pair of 2 cm² samples of the hydrogel, the authors demonstrate that an adult human weighing 87 kg can be suspended from the adhesive rig. Additionally, the authors used a structured PHEMA gel pad to detach the wing scales of morpho butterflies without damaging the scales' gossamer microstructures—a task too delicate for liquid glues. According to the authors, the PHEMA hydrogel can be scaled up and chemically modified for an array of applications. — P.N.

Improving functional recovery after stroke

Stroke is a major cause of disability, and the lack of an effective therapy that promotes long-term recovery represents an unmet medical need. Angiogenesis, or the formation of new blood vessels, has been proposed as a therapeutic target, but treatments that promote angiogenesis after cerebral stroke are lacking. Ruslan Rust et al. (pp. 14270–14279) provide evidence in mice that blocking a molecule called Nogo-A, which inhibits angiogenesis and the growth of neuronal projections, promotes vascular and neural repair as well as functional recovery after ischemic stroke, which occurs when an artery that supplies oxygen-rich blood to the brain becomes

blocked. Both genetic deletion of Nogo-A and treatment with an antibody that blocks Nogo-A increased the number of newly formed blood vessels and improved behavioral performance on motor tasks assessing stroke-affected limb function 3 weeks after injury. Treatment with the anti-Nogo-A antibody also improved the survival of neurons and connections between neurons, increased levels of the neurotransmitter dopamine, which plays a key role in motor function and recovery, and increased the density of nerve fibers near the damaged tissue 3 weeks after injury. According to the authors, anti-Nogo-A antibodies, including an antibody in clinical testing for spinal cord injury, could represent an angiogenesis-promoting therapeutic strategy for ischemic stroke. — J.W.

Dung beetles use a flexible compass for spatial orientation

South African dung beetles sequester food by shaping pieces of dung into spheres that are spirited away from competitors in the savanna. To hasten their getaway, the beetles scurry in a straight line away from the dung pile, using the sun's position to align themselves as they haul their meal. However, as the midday sun rises in the sky, the beetles' ability to draw positional cues from it wanes. To determine how the beetles maintain their heading despite being deprived of this crucial cue, Marie Dacke et al. (pp. 14248–14253) tested the beetles' behavior under a series of controlled solar elevations and wind speeds in outdoor and indoor arenas. At high solar elevations, the beetles relied on a wind compass, rather than the sun's position, to find their bearing; the authors monitored wind direction and speed in the beetles' natural habitat and found that the speed peaks when the sun is at its zenith. Wind cues improved the precision of the beetles' orientation. Compared with beetles with intact antennae, beetles whose antennae had been amputated oriented poorly along a given direction, suggesting that the beetles perceive mechanosensory cues using their antennae, likely mediated by a structure called the Johnston organ. Importantly, the beetles were capable of transferring sensory cues



Dung beetle. Image courtesy of Chris Collingridge (photographer).

between the sun and wind compasses depending on solar elevation, suggesting a composite compass snapshot undergirded by a common neural network for spatial memory. The findings uncover the role of a flexible, multisensory compass for spatial orientation in dung beetles, according to the authors. — P.N.

Bubble pinch-off in confined conditions

The pinch-off of a bubble involves formation of a singularity, which is expected to be independent of the details of the experimental setup and thus to exhibit

universal dynamics. However, bubble pinch-off has been shown to be nonuniversal when it occurs in a large tank of viscous liquid. Amir Pahlavan et al. (pp. 13780–13784) explored the dynamics of bubble formation and pinch-off in the highly confined conditions within a capillary tube. Whereas in a large tank the neck of the bubble contracts linearly with time, the neck of the bubble in a capillary tube contracted in 2 distinct stages. Initially the neck radius varied



Sequence of snapshots showing neck shrinkage and eventual bubble pinch-off in a capillary tube.

with the $1/5$ power of time, before transitioning to a linear dependence on time shortly before pinch-off. Unlike the case of liquid in a large tank, bubble formation in the capillary tube was insensitive to the details of the experimental conditions. The first stage of pinch-off, driven by movement of the contact line where liquid, gas, and solid phases meet, effectively erases the memory of the system, leading to universal dynamics. According to the authors, the results have implications for bubble and drop formation in confined conditions, such as in microfluidic technology and geophysics. — B.D.

Nanoparticles underlie optical effects of earliest photographs

The daguerreotype is the earliest photographic technology that successfully captured an image from a camera, with extraordinary resolution and clarity even by current standards. The preservation of daguerreotypes, which are records of history and culture, requires an understanding of the physical and chemical mechanisms underlying their optical response. Andrea Schlather et al. (pp. 13791–13798) combined daguerreotype artistry and expertise, experimental nanoscale surface analysis, and electromagnetic simulations to perform a comprehensive analysis of these early photographs. The findings showed that the

scattering spectrum of individual nanoparticles on the daguerreotype surface consists of a narrow, blue/UV peak as well as a broader red peak. As a result, the daguerreotype exhibits a blue tone when viewed from above, but the tone shifts to brown/red as the



Ramesseum, Thebes, 1844. Girault de Prangey, The Metropolitan Museum of Art. Purchase, Mr. and Mrs. John A. Moran Gift, in memory of Louise Chisholm Moran, Joyce F. Menschel Gift, Joseph Pulitzer Bequest, 2016 Benefit Fund, and Gift of Dr. Mortimer D. Sackler, Theresa Sackler and Family, 2016 (2016.604).

viewing angle increases. Moreover, the scattering spectrum of the nanostructure is strongly affected by particle morphology and size, but not composition. For example, decreasing nanoparticle height leads to a blueshift in the spectrum, whereas increasing overall nanoparticle dimensions causes a redshift and broadening of the spectral peak and diminishes the angle-dependent color effect. According to the authors, these insights could be used to develop preservation protocols and novel color printing technologies. — J.W.

Origin and diversification of sunflower family

The sunflower family, composed of an estimated 25,000–30,000 species, accounts for nearly 10% of all flowering plants. Global in distribution, the family occupies nearly every type of habitat on Earth and is marked by a complex inflorescence as seen in the North American sunflower, in which individual flowers are clustered to mimic a single large flower to lure pollinators. However, the origins, migration routes, and patterns of diversification that led to the family's ecological success remain unclear.

Using phylogenetic analysis of nearly 1,000 genomic locations in around 250 species, Jennifer Mandel et al. (pp. 14083–14088) found that the family likely originated around 83 million years ago in the Late Cretaceous Period in southern South America. The earliest diversification out of South America may have occurred around 56 million years ago, during a period of dramatic climate change. Subsequently, the family rampantly diversified during the middle-to-late Eocene Epoch, 42–37 million years ago, a period marked by global cooling, resulting in more than 95% of existing species. Biogeographical analysis suggests that the family migrated to North America, south and central Africa, and Asia, with ancestral range estimates suggesting different possible dispersal routes out of South America. Regardless of the actual route, the family's prolific diversification and global colonization likely began once it reached Africa around 42 million years ago. According to the authors, the findings illuminate the evolutionary processes underlying the wide reach and vibrant diversity of a major group of flowering plants. — P.N.



Werneria pumila Kunth, an endemic South American genus that resulted from explosive diversification out of Africa in the middle Eocene.